

Molecular ion abundances in the diffuse ISM: CF⁺, HCO⁺, HOC⁺, and C₃H⁺*

M. Gerin¹, H. Liszt², D. Neufeld³, B. Godard¹, P. Sonnentrucker^{4,5}, J. Pety⁶, and E. Roueff⁷

¹ Sorbonne Université, Observatoire de Paris, Université PSL, École normale supérieure, CNRS, LERMA, 75014 Paris, France
e-mail: maryvonne.gerin@ens.fr

² National Radio Astronomy Observatory, 520 Edgemont Road, Charlottesville, VA 22903, USA

³ Department of Physics & Astronomy, Johns Hopkins University, 3400 N. Charles St., Baltimore, MD 20218, USA

⁴ Space Telescope Science Institute, Baltimore, MD 21218, USA

⁵ European Space Agency, Paris, France

⁶ Institut de Radioastronomie Millimétrique (IRAM), 300 rue de la Piscine, 38406 Saint-Martin-d'Hères, France

⁷ Sorbonne Université, Observatoire de Paris, Université PSL, École normale supérieure, CNRS, LERMA, 92190 Meudon, France

Received 16 June 2018 / Accepted 26 October 2018

ABSTRACT

Aims. The transition between atomic and molecular hydrogen is associated with important changes in the structure of interstellar clouds, and marks the beginning of interstellar chemistry. Most molecular ions are rapidly formed (in ion–molecule reactions) and destroyed (by dissociative recombination) in the diffuse ISM. Because of the relatively simple networks controlling their abundances, molecular ions are usually good probes of the underlying physical conditions including, for instance the fraction of gas in molecular form or the fractional ionization. In this paper we focus on three possible probes of the molecular hydrogen column density, HCO⁺, HOC⁺, and CF⁺.

Methods. We presented high-sensitivity ALMA absorption data toward a sample of compact H II regions and bright QSOs with prominent foreground absorption, in the ground-state transitions of the molecular ions HCO⁺, HOC⁺, and CF⁺ and the neutral species HCN and HNC, and from the excited-state transitions of C₃H⁺ (4-3) and ¹³CS(2-1). These data are compared with *Herschel* absorption spectra of the ground-state transition of HF and p-H₂O.

Results. We show that the HCO⁺, HOC⁺, and CF⁺ column densities are well correlated with each other. HCO⁺ and HOC⁺ are tightly correlated with p-H₂O, while they exhibit a different correlation pattern with HF depending on whether the absorbing matter is located in the Galactic disk or in the central molecular zone. We report new detections of C₃H⁺ confirming that this ion is ubiquitous in the diffuse matter, with an abundance relative to H₂ of $\sim 7 \times 10^{-11}$.

Conclusions. We confirm that the CF⁺ abundance is lower than predicted by simple chemical models and propose that the rate of the main formation reaction is lower by a factor of about 3 than usually assumed. In the absence of CH or HF data, we recommend to use the ground-state transitions of HCO⁺, CCH, and HOC⁺ to trace diffuse molecular hydrogen, with mean abundances relative to H₂ of 3×10^{-9} , 4×10^{-8} , and 4×10^{-11} , respectively, leading to sensitivity $N(\text{H}_2)/\int \tau d\nu$ of 4×10^{20} , 1.5×10^{21} , and $6 \times 10^{22} \text{ cm}^{-2}/\text{km s}^{-1}$, respectively.

Key words. ISM: general – ISM: clouds – ISM: molecules – radio lines: ISM

1. Introduction

The diffuse interstellar medium is ubiquitous in the Galaxy, and exhibits a complex structure with a mixing of phases with widely different conditions. Dust extinction provides the total column density of material, which can be inverted to yield the three-dimensional structure when the number of background target stars is sufficient (e.g., Lallement et al. 2014; Green et al. 2015). Such recent surveys confirm the mixing of phases with the dense structure embedded in bubbles of low density material. However, the extinction data do not provide information about the composition of the absorbing gas. Classical spectroscopic tracers are commonly used for detecting emission lines from ionized gas (H α), atomic gas (H I), or molecular gas (CO), but they usually miss the diffuse molecular gas when the CO ($J = 1 \rightarrow 0$) emission is not strong enough to be detected. This

so-called “CO-dark gas” because its CO emission is not detected contributes to the total γ -ray production (e.g., Remy et al. 2017), dust extinction, or emission (Planck Collaboration XXIV 2011), and [C II] fine structure line emission (Pineda et al. 2013).

The CO-dark gas usually surrounds the molecular clouds detected in CO (Wolfire et al. 2010; Remy et al. 2017). Indeed, molecular clouds are known to occupy a small fraction of the Galaxy volume, although they represent most of the dense gas mass. The transition region between fully molecular and fully atomic gas extends over larger areas on the sky and accounts for a significant, although not dominant, fraction of the neutral gas mass at the Galaxy scale, $\sim 30\%$ (Pineda et al. 2013). These authors have used *Herschel* data and performed a careful separation of the contributions of the neutral and molecular ISM phases by comparing the [C II] emission with that of H I and CO. To derive column densities from the emission line intensities, these authors have made standard assumptions on the H I spin temperature, and on the scaling of CO ($J = 1 \rightarrow 0$) emission with the H₂ column density. Both methods have

* The continuum divided spectra are only available at the CDS via anonymous ftp to cdsarc.u-strasbg.fr (130.79.128.5) or via <http://cdsarc.u-strasbg.fr/viz-bin/qcat?J+A+622/A26>

their own uncertainties which propagate in the derivation of the fraction of molecular gas not traced by CO. Alternative tracers are therefore needed which can probe the diffuse gas, be easily accessible from the ground, and provide an independent estimation of the diffuse molecular gas properties.

Absorption spectroscopy provides an alternative means for separating the ISM phases. In low density regions, the excitation of molecular energy levels is dominated by the cosmic background radiation. Therefore, the derivation of line opacities and molecular column densities is straightforward and accurate. As summarized by [Snow & McCall \(2006\)](#), UV and visible spectroscopy have been extensively used to probe the properties of the diffuse and translucent gas, understand the mechanisms that control the transition from atomic to molecular gas, and investigate the composition and physical conditions of the diffuse molecular gas including the CO-dark regions (e.g., [Spitzer & Jenkins 1975](#); [Sheffer et al. 2008](#); [Rachford et al. 2009](#); [Jenkins & Tripp 2011](#)). Similarly, absorption spectroscopy has been successfully used to probe the structure and chemistry of the diffuse interstellar medium at radio wavelengths for decades ([Goss 1968](#); [Whiteoak & Gardner 1970](#); [Lucas & Liszt 1996](#)). The ground-state line of hydrides observed with the *Herschel* satellite provided a wealth of new information on the properties of the diffuse interstellar gas ([Gerin et al. 2016](#)), including sensitive tracers of molecular gas (HF, CH, and H₂O), of the cosmic ray ionization rate (OH⁺, H₂O⁺, H₃O⁺), and strong supporting evidence for the role of turbulent dissipation in triggering the formation of the first molecule building blocks like CH⁺ and SH⁺ ([Godard et al. 2012, 2014](#)). The GREAT receiver on SOFIA has enabled further studies of CH, OH, and SH absorption ([Neufeld et al. 2015](#); [Wiesemeyer et al. 2016, 2018](#)).

Among the interstellar molecules, fluorine species are particularly attractive molecular diagnostics because of the simplicity of fluorine chemistry. Fluorine atoms are unique because they can react exothermically with H₂ to form HF, the only neutral diatomic hydride which is more strongly bound than H₂. As a consequence theoretical models predict that HF will become the dominant fluorine reservoir in molecular gas, a prediction fully confirmed by the *Herschel* observations ([Sonnentrucker et al. 2015](#)). HF is destroyed mainly by reactions with C⁺, forming CF⁺. Hence, CF⁺ is expected to be the second most important fluorine reservoir in regions where C⁺ is abundant, and it is expected to account for a few percents of the gas-phase fluorine abundance. First detected in the Orion Bar ([Neufeld et al. 2006](#)), CF⁺ has been shown to be present in the diffuse ISM ([Liszt et al. 2014, 2015](#)), with a somewhat lower abundance (by a factor of ~4) than the theoretical predictions.

HCO⁺ and HOC⁺ are two interesting ions that are widespread in the diffuse interstellar medium. While HCO⁺, the most stable isomer, has been shown from observations to be a good tracer of molecular hydrogen since 20 years ([Lucas & Liszt 1996](#)), the absorption becomes saturated at H₂ column densities corresponding to translucent gas, with visual extinction between 1.5 and 3 mag ([Snow & McCall 2006](#)). It is therefore interesting to look for complementary tracers with different sensitivities to the molecular hydrogen column allowing to probe a broader range of H₂ column densities. The less stable isomer HOC⁺ may be such an alternative tracer. With an abundance ratio to HCO⁺ at the percent level ([Liszt et al. 2004](#)), HOC⁺ is thought to be mainly formed by the chemical reaction of C⁺ with H₂O, whose secondary channel leads to HCO⁺. Therefore, HCO⁺ and HOC⁺ are expected to coexist in the diffuse molecular gas.

Another interesting property of CF⁺ and HOC⁺ is their expected close relationship to their parent species, C⁺ and HF for CF⁺, and C⁺ and H₂O for HOC⁺. At submillimeter wavelengths, Galactic HF and H₂O cannot be detected from the ground because of the high opacity of the atmosphere at the frequencies of their ground-state rotational transitions. Also, the ground electronic transitions for HF and H₂O occur in the FUV around 950 Å for HF and 1240 Å for H₂O but the combination of weak band strength and blending with adjacent atomic species renders their detection and study very challenging even from space. The ground-state transitions of the three molecular ions discussed here are located at millimeter wavelengths where the atmospheric transmission is excellent. We have therefore performed observations with ALMA of sources previously observed with *Herschel* to probe how the ions and neutral species are related and whether the HCO⁺, HOC⁺, and CF⁺ molecular ions could be used as surrogates for either the hydride species or molecular hydrogen.

The observations are described in Sect. 2 and analyzed in Sect. 3. Section 4 presents the resulting abundances relative to H₂ and the implication for the chemistry of diffuse gas are discussed in Sect. 5. Section 6 discusses the ways in which gas near the Galactic center differs from that in the disk. Section 7 summarizes the main conclusions.

2. ALMA observations

We present ALMA Cycle 2 observations under project 2013.1.1194.S: The targeted sources are listed in Table 1. Some of the observations under this project were previously presented by [Gerin & Liszt \(2017\)](#) who discussed absorption from gas in the Galactic bulge that is seen toward the quasar background target B1741-312.

Observations were divided in three scheduling blocks that have been observed separately in different interferometer configurations between 2014 and 2015. We used a configuration of the ALMA correlator allowing simultaneous observations of the lines listed in Table 2 using the two available sidebands, with spectral resolution set to 61.03 kHz (0.18 km s⁻¹) for CF⁺, 122.07 kHz (0.4 km s⁻¹) for HOC⁺, and 244.14 kHz (0.8 km s⁻¹) for HCN, HNC, HCO⁺, c-C₃H, ¹³CS, and C₃H⁺. A 1.875 GHz wide spectral window with a coarse spectral resolution of 15.6 MHz was reserved for detecting the continuum emission at 102 GHz with high sensitivity. The bandpass calibrators were J1427-4206, J1717-3342, J1924-2914, and the phase calibrator was J1752-2956. As flux calibrator the solar system objects Titan, Venus, and Ceres were used. The system attempted with success to use B1730-130 aka J7133-1304, one of the program targets, as bandpass calibrator and data affected by this problem were masked. The data were calibrated and deconvolved using CASA and the resulting data cubes were then exported to GILDAS for further analysis.

Table 1 lists the continuum values at 102 GHz derived from the spectral window dedicated to the detection of the continuum. The 102 GHz continuum window was used only for phase calibration. The continuum level to be subtracted to measure the strength of the absorption was determined separately in each spectral window. Images of the four extended sources (G0.02-00.7, SgrB2, G5.89-0.4, G10.62-0.4) are shown in Fig. A.1. Absorption spectra have been extracted at the peak of the continuum maps or using weighted average of bright pixels with minimum line contamination from the background source. The positions of the extracted spectra are listed in Table 1. The

Table 1. Summary of observations.

Source ^a	RA ^a (J2000)	Dec ^a (J2000)	RA _s ^b (J2000)	Dec _s ^b (J2000)	V _{LSR} ^c km s ⁻¹	Beam "	F _s ^d Jy/beam	σ ^e %
B1730-130	17:33:02	-13:04:49	17:33:02.7	-13:04:49	-	3.7 × 1.7	1.9	0.32
G5.89-0.4	18:00:30	-24:04:00	18:00:30.4	-24:04:01.3	9.0	1.0 × 0.6	0.34	0.28
G10.62-0.4	18:10:28	-19:55:50	18:10:28.7	-19:55:50	-0.4	0.9 × 0.6	0.46	0.3
SgrB2-M	17:47:20	-28:23:45	17:47:20.3	-28:23:05	60	2.7 × 1.8	2.8	0.4
SgrB2-S	17:47:20	-28:23:45	17:47:20.4	-28:23:45	60	2.7 × 1.8	0.58	0.7
G0.02-0.07 ^f	17:45:51	-28:59:50	17:45:51.9	-28:59:27	50	2.7 × 1.8	0.02	6.3
	17:45:51	-28:59:50	17:45:52.1	-28:59:41	50	2.7 × 1.8	0.008	15
	17:45:51	-28:59:50	17:45:52.4	-29:00:03	50	2.7 × 1.8	0.01	13
	17:45:51	-28:59:50	17:45:51.6	-29:00:22	50	2.7 × 1.8	0.03	13
B1741-312	17:44:23	-31:16:35	17:44:23.6	-31:16:36	-	2.6 × 1.9	0.55	0.6

Notes. ^(a)Field center. ^(b)Position of the extracted spectrum. ^(c)LSR Velocity of the molecular gas associated with the source. ^(d)Continuum value at 102 GHz at the position of the extracted spectrum. ^(e)Mean noise level on the continuum at 1 km s⁻¹ spectral resolution, expressed as percentage of the continuum intensity. ^(f)G0.02-0.07 is part of the SgrA molecular complex. The sources are displayed according to the completion of observations.

absorption spectra have been obtained by dividing the observed spectra by the continuum intensity in the same band. For further analysis the data have been smoothed at a spectral resolution of 1 km s⁻¹. Except for the very weak sources in the G0.02-0.07 field, we obtain a noise level between 0.2 and 0.6% of the continuum brightness when smoothed at the common velocity resolution of 1 km s⁻¹, allowing the detection of very weak features.

Figure 1 presents the ion spectra, and Fig. B.1 shows the whole set of spectra. The continuum emission of the compact H II regions in the field of G0.02-0.07 are too weak for detecting weak absorption features produced by HOC⁺ and CF⁺. Only the strongest features produced by HCO⁺, HCN, and HNC have been detected. The data toward the compact sources in the G0.02-0.07 field will not be further discussed.

Toward both G5.89-0.4 and G10.62-0.4, which have ultra-compact H II regions, the CF⁺ data are contaminated by the emission of the H66ε hydrogen recombination line, which was already seen in the W49N analysis of Liszt et al. (2015). We chose a position away from the brightest continuum and fitted the broad hydrogen recombination line with a Gaussian profile. Other hydrogen recombination lines are detected, notably the H59γ at 89.1985450 GHz which is blueshifted by 10 MHz (33 km s⁻¹) from the HCO⁺(1-0) transition. The hydrogen recombination line emission is associated with the bright free-free continuum emission, and is absent in the QSO spectra. Because H66ε is redshifted relative to CF⁺, it does not contaminate the data toward SgrB2 where the line of sight absorption is blue-shifted relative to the main envelope.

A faint and broad absorption from C₃H⁺ is detected at velocities between 15 and 45 km s⁻¹ corresponding to the diffuse gas along the line of sight to the G10.6-0.4 H II region, with a superimposed narrow feature at 35 km s⁻¹. A second narrow feature is present outside the expected spectral range of the foreground absorption near -167 km s⁻¹ (not displayed here). While these narrow absorption lines are real, they are not produced by C₃H⁺, but are associated with molecular lines from the hot molecular core next to G10.6-0.4, because we detect weak emission at the same frequency a few pixels away from the bright continuum emission. Similar narrow absorption features are detected towards G10.62-0.4 in the HCN and HOC⁺ spectral windows,

notably a rather strong feature at 124 km s⁻¹, not displayed here. We used Splatalogue¹ and the CDMS² and JPL³ line catalogs for line identification and assignment. We assigned the narrow feature appearing at 124 km s⁻¹ in the HCN spectral window to the CH₃OH 15(3,13)–14(4,10) line at 88594.4809 MHz, leading to a LSR velocity of -1.2 km s⁻¹ for this narrow absorption feature. Then, the two narrow features detected in the C₃H⁺ spectrum can be assigned to two transitions of g-CH₃CH₂OH, the 10(0,10)–10(1,10) line at 89947.016 MHz ($E_l = 70.98$ cm⁻¹) for the 35 km s⁻¹ feature and the 13(1,12)–13(1,13) line at 90007.685 MHz ($E_l = 90.9$ cm⁻¹) for the -167 km s⁻¹ feature. The spectroscopy of CH₃CH₂OH is well known, because it has been studied by Pearson et al. (2008) and revised by Müller et al. (2016). We have fit the narrow absorption lines with Gaussian profiles, and used the residual to estimate the absorption due to C₃H⁺ along the G10.62-0.4 line of sight.

The column densities have been derived by integrating the line opacity over selected velocity intervals, either 1 km s⁻¹ for the comparison of the line profiles or broader intervals as listed in Table 3 for deriving column densities associated with individual velocity features. Because the analysis is focused on the diffuse gas, we have assumed that the level population is in equilibrium with the Cosmic Microwave Background. This hypothesis is justified by the low density of the medium as discussed for instance by Liszt & Gerin (2016) for the G10.62-0.4 sight-line. We recall the expression for the coefficient $N/\int \tau dv$ for a ground-state transition:

$$N = Q(T_{\text{ex}}) \frac{8\pi\nu^3}{c^3} \frac{1}{g_u A_{ul}} \left[1 - e^{-\frac{h\nu}{k_B T_{\text{ex}}}} \right]^{-1} \int \tau dv, \quad (1)$$

where T_{ex} is the excitation temperature, $Q(T_{\text{ex}})$ the partition function, A_{ul} the Einstein coefficient of the transition of frequency ν between the upper and lower levels of degeneracies g_u and g_l . The coefficients we have used are listed in the last column of Table 2.

¹ www.cv.nrao.edu/php/splat/advanced.php

² www.astro.uni-koeln.de/cdms

³ spec.jpl.nasa.gov

Table 2. Observed lines.

Species	Transition	Frequency MHz	A		$N/\int \tau dv^a$ $10^{12} \text{ cm}^{-2}/\text{km s}^{-1}$
			10^{-5} s^{-1}		
HCO ⁺	1–0	89188.525	4.19		1.11
HOC ⁺	1–0	89487.414	2.13		2.19
CF ⁺ ^b	1–0	102587.533	0.48		13.5
C ₃ H ⁺	4–3	89957.625	3.39		16.2
c-C ₃ H	2(1,2)5/2, 3–1(1,1)3/2, 2	91494.349	1.55		14.3
¹³ CS	2–1	92494.257	1.18		9.72
HCN ^b	1–0	88631.601	2.41		1.91
HNC	1–0	90663.564	2.69		1.78
NH ₂ CHO ^b	2(1,2)–1(0,1)	102217.572	0.27		114

Notes. ^(a)For an excitation temperature equal to the CMB, 2.725 K, ^(b)for the combined hyperfine components. A recent determination of the rest frequency has been published by [Stoffels et al. \(2016\)](#).

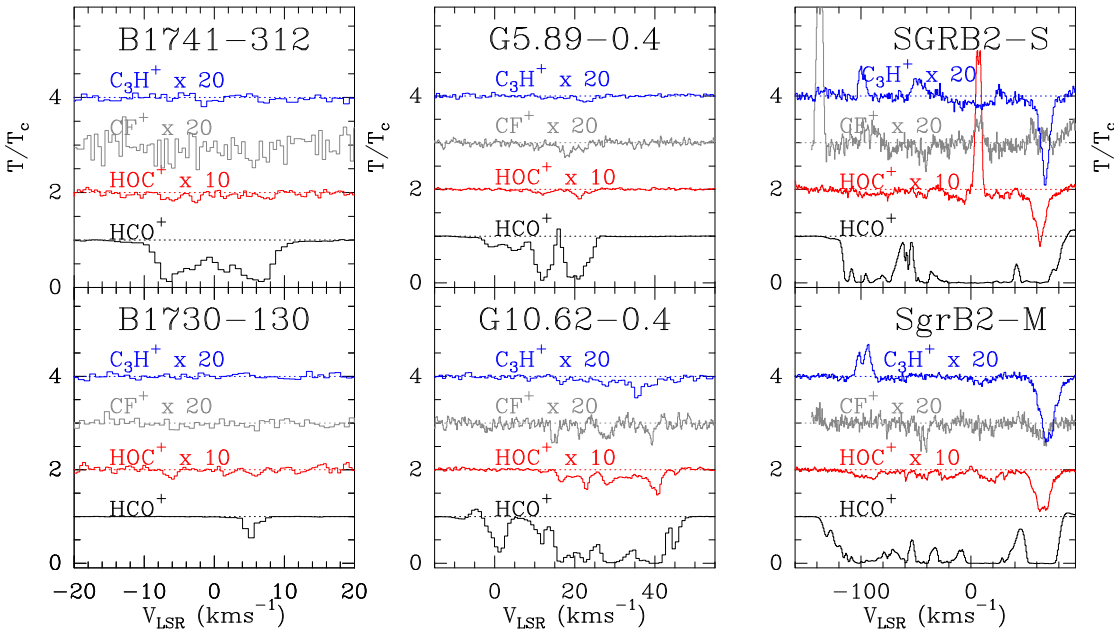


Fig. 1. Presentation of the molecular ion spectra toward the target sources at the peak of the continuum emission. The data are displayed as line to continuum ratio, and shifted vertically for clarity. The weak absorption lines have been multiplied by the indicated scaling factors: 20 for C₃H⁺ and CF⁺ and 10 for HOC⁺.

3. Results

3.1. HOC⁺ and HCO⁺

As illustrated in Figs. 1 and 2, the profiles of HCO⁺ and HOC⁺ are similar, confirming that these species are closely related to each other in diffuse gas. We have compared the absorption profiles of both ions with those of p-H₂O and HF detected by *Herschel* ([Sonnentrucker et al. 2015](#)). Figure 2 presents a comparison of the line profiles for the case of G10.62-0.4, while Figure 3 presents channel by channel comparisons for all sources. Each point in this figure represents a 1 km s⁻¹ velocity channel, the red points correspond to the G10.6-0.4 line of sight, the blue points to G5.89-0.4, the green points to the QSO sight-lines, and the gray points to SgrB2-S. This plot only shows data corresponding to the material along the line of sight, namely, velocities higher than 8 km s⁻¹ for G10.6-0.4, 15.5 km s⁻¹ for G5.89-0.4 and lower than -20 km s⁻¹ for SgrB2-S. We have not applied any restriction for the QSO sight-lines. It is remarkable that, when comparing HCO⁺ with p-H₂O, all sources lay on the same relationships, while SgrB2-S stands out when HF or CF⁺ are compared with HCO⁺ or with p-H₂O. When compared with

p-H₂O or with HCO⁺, the HOC⁺ absorption toward SgrB2-S is somewhat fainter than toward the sources in the Galactic plane, but the difference is not as strong as with HF. Differences between the Galactic center and Galactic disk gases are discussed in more detail in Sect. 6.

The relationships between p-H₂O and HCO⁺ and p-H₂O and HOC⁺, like that between HCO⁺ and HOC⁺, are nearly linear. Because of the different behavior of the gas in the Galactic Center, we have restricted the correlation analysis to the G10.62-0.4 and G5.89-0.4 sight-lines. This will also allow us to use a consistent sample for all species, those observed with *Herschel* like p-H₂O and HF, and those observed with ALMA. We obtained the following relationships from least square fits, assuming the column densities are proportional to each other and restraining the fit to points with signal-to-noise ratio (S/N) greater than 2.5 σ and opacity lower than 3.5:

$$N(\text{HCO}^+) = (0.47 \pm 0.03) N(\text{p-H}_2\text{O}), \quad (2)$$

$$N(\text{HOC}^+) = (7.4 \pm 1.5) \times 10^{-3} N(\text{p-H}_2\text{O}), \quad (3)$$

$$N(\text{HOC}^+) = (1.5 \pm 0.3) \times 10^{-2} N(\text{HCO}^+). \quad (4)$$

Table 3. Column densities.

Source km s^{-1}	$N(\text{HOC}^+)$ 10^{12} cm^{-2}	$N(\text{CF}^+)$ 10^{12} cm^{-2}	$N(\text{C}_3\text{H}^+)$ 10^{12} cm^{-2}	$N(\text{HCO}^+)$ 10^{12} cm^{-2}	$N(\text{c-C}_3\text{H})$ 10^{12} cm^{-2}	$N(\text{HNC})$ 10^{12} cm^{-2}	$N(^{13}\text{CS})$ 10^{12} cm^{-2}
G10.62-0.4							
[7, 21]	0.26 ± 0.02	0.54 ± 0.15	0.38 ± 0.16	16.7 ± 0.5	1.7 ± 0.4	6.4 ± 0.9	0.39 ± 0.1
[21, 26]	0.22 ± 0.01	1.0 ± 0.1	0.25 ± 0.10	10.5 ± 0.3	1.4 ± 0.4	5.9 ± 0.9	0.21 ± 0.05
[26, 35]	0.39 ± 0.02	0.53 ± 0.12	0.90 ± 0.16	26.6 ± 0.7	0.9 ± 0.4	14 ± 1	0.52 ± 0.06
[35, 43]	0.44 ± 0.02	0.40 ± 0.11	0.81 ± 0.16	36.1 ± 5.5	1.4 ± 0.4	11 ± 1	0.16 ± 0.06
[43, 50]	<0.05	<0.3	<0.3	2.7 ± 0.1	<1.0	0.96 ± 0.2	<0.15
G5.89-0.4							
[15, 25]	0.15 ± 0.02	0.96 ± 0.13	0.45 ± 0.1	12.7 ± 0.5	1.3 ± 0.2	5 ± 0.9	<0.6
B1741-312							
[-7, 7]	0.23 ± 0.05	0.81 ± 0.4	<0.5	23 ± 0.5	–	5.5 ± 0.2	–
B1730-130							
[0, 10]	0.06 ± 0.02	0.06 ± 0.03	<0.2	1.2 ± 0.1	–	0.05 ± 0.02	–

Notes. The first column gives the velocity intervals used for deriving the various molecular column densities listed in the other columns.

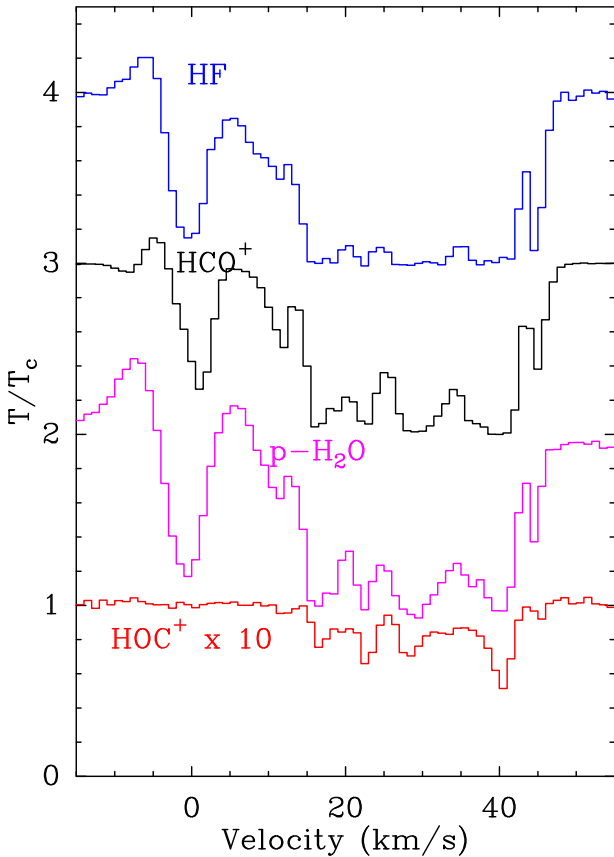


Fig. 2. Comparison of absorption spectra toward G10.62-0.4 obtained with *Herschel* ($\text{p-H}_2\text{O}$ and HF) and with ALMA (HCO^+ and HOC^+) at the same velocity resolution of 1 km s^{-1} . The spectra have been displaced vertically for clarity. The HOC^+ spectrum is scaled by a factor of 10. The velocity range between -10 and 10 km s^{-1} corresponds to the molecular gas associated to the G10.6-0.4 H II region, while the foreground absorption can be seen between 10 and 50 km s^{-1} . Despite the huge difference in angular resolution, the absorption spectra are very similar.

The excellent correlation between HCO^+ and H_2O was already discussed in the context of the SWAS and ODIN missions, using the ground-state $\text{o-H}_2\text{O}$ line at 557 GHz

(Neufeld et al. 2002; Plume et al. 2004), while Lucas & Liszt (1996) showed that HCO^+ and OH absorption were tightly correlated. A tight correlation between HCO^+ and H_2O is therefore expected, and clearly seen in the data.

As for HOC^+ , Liszt et al. (2004) observed HCO^+ and HOC^+ toward three QSOs with the Plateau de Bure Interferometer (PdBI) and derived a mean ratio of $N(\text{HOC}^+)/N(\text{HCO}^+) \sim 0.01$, similar to the ALMA measurement, although with larger uncertainties. The new detections obtained with ALMA toward B1741-312 and B1730-130 follow the same relationship as previous measurements obtained with PdBI and allow a more precise determination of the $N(\text{HOC}^+)/N(\text{HCO}^+)$ abundance ratio of $(1.5 \pm 0.3) \times 10^{-2}$. Liszt et al. (2004) derived $N(\text{HOC}^+)/N(\text{OH}) = 3 - 6 \times 10^{-4}$ by comparing the Plateau de Bure data with absorption measurements of the OH Λ doubling lines at 18 cm . The recent analysis of SOFIA and *Herschel* observations performed by Wiesemeyer et al. (2016) provides an independent means to relate the OH and H_2O column densities. These authors obtained $N(\text{OH})/N(\text{p-H}_2\text{O}) \sim 16$ or $N(\text{OH})/N(\text{H}_2\text{O}) \sim 4$ using an ortho-to-para ratio of 3 for H_2O (Flagey et al. 2013). The new ALMA measurements therefore predict $N(\text{HOC}^+)/N(\text{OH}) \sim 4.5 \times 10^{-4}$, in good agreement with the independent determination toward distant QSOs.

We have also compared HCO^+ and HOC^+ with HF. As illustrated in Fig. 3, the velocity channels belonging to the SgrB2-S sightline lead to different relationships than those toward G10.6-0.4 and G5.89-0.4. A similar behavior has been noticed by Sonnentrucker et al. (2013) for HF and $\text{p-H}_2\text{O}$, where an excess of water vapor absorption relative to HF was detected for the molecular gas in the vicinity of the Galactic Center. The excess of HCO^+ and HOC^+ absorption relative to HF for gas in the Galactic Center appears therefore as another consequence of the tight relationships between $\text{p-H}_2\text{O}$ and HCO^+ , and to a lesser extent because of the limited number of velocity channels where both species are detected, between $\text{p-H}_2\text{O}$ and HOC^+ . We obtained the mean relationships for Galactic disk diffuse gas:

$$N(\text{HCO}^+) = (0.25 \pm 0.05) N(\text{HF}), \quad (5)$$

$$N(\text{HOC}^+) = (4 \pm 1.5) \times 10^{-3} N(\text{HF}). \quad (6)$$

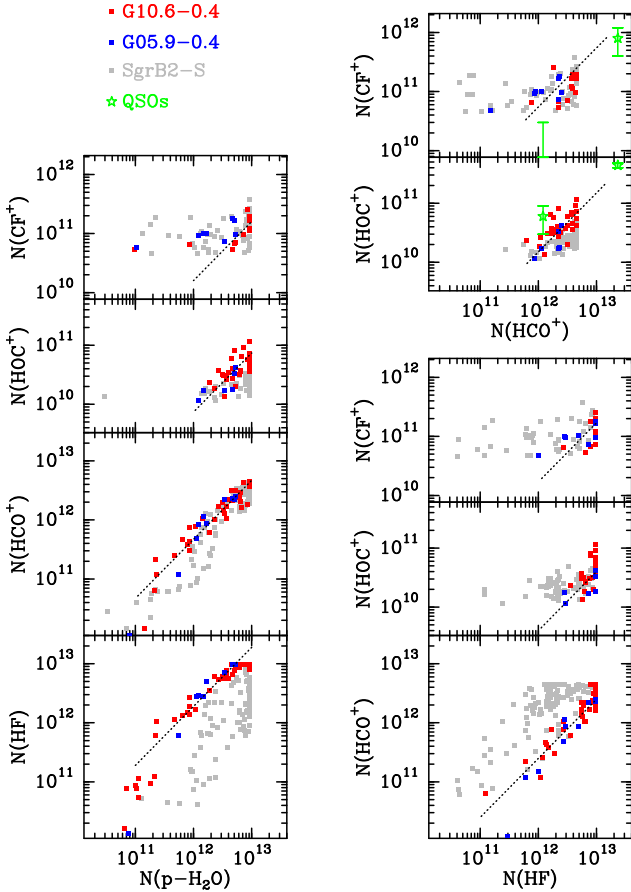


Fig. 3. Comparison of the column densities in 1 km s^{-1} velocity bins for the program sources. Data for SgrB2-S are plotted in gray, G10.62-0.4 in red, G5.89-0.4 in blue and those toward B1730-130 and B1741-312 in green with error bars. The dotted lines show the mean relationships discussed in the text. The HF and p-H₂O data have been obtained with *Herschel* (Sonnentrucker et al. 2015), the other data are from ALMA. The velocity range corresponding to the background sources are excluded. Only data points with S/N greater than 2.5σ , and with opacity lower than 3.5 are shown.

3.2. CF⁺

Because the CF⁺ absorption is very weak, while the HF lines are heavily saturated, there are very few velocity channels for which CF⁺ and HF can be compared, leading to a relatively high uncertainty on the abundance ratio. We also show a comparison of the CF⁺ column density with that of p-H₂O and of HCO⁺ in Fig. 3. A first comparison of CF⁺ and HF based on NOEMA and *Herschel* observations of the line of sight toward the massive star forming region W49 has been presented by Liszt et al. (2015). They found that CF⁺ is well correlated with HF as expected but that the mean ratio is lower by a factor of ~ 4 than the predicted value of $\sim 1/20$ using the reaction rates by Neufeld & Wolfire (2009) listed in Table C.1. Our results obtained using the G10.62-0.4 and G5.89-0.4 sight-lines support the previous measurements with

$$N(\text{CF}^+) = (1.7 \pm 0.3) \times 10^{-2} N(\text{HF}) \quad (7)$$

We also obtain the following mean relationships with HCO⁺, HOC⁺, and p-H₂O:

$$N(\text{CF}^+) = (5.5 \pm 1) \times 10^{-2} N(\text{HCO}^+), \quad (8)$$

$$N(\text{CF}^+) = (2.5 \pm 0.7) N(\text{HOC}^+), \quad (9)$$

$$N(\text{CF}^+) = (1.6 \pm 0.5) \times 10^{-2} N(\text{p-H}_2\text{O}). \quad (10)$$

3.3. C₃H⁺

The molecular ion C₃H⁺ has been first identified in the ISM as the carrier of a series of unidentified lines in the Horsehead nebula WHISPER line survey (Pety et al. 2012), and then detected in PDRs like the Orion Bar (Cuadrado et al. 2015) and along the line of sight to SgrB2 (McGuire et al. 2013). Guzmán et al. (2015) have imaged its spatial distribution at the Horsehead nebula edge and conclude that C₃H⁺ behaves as a precursor of hydrocarbons, and that its chemistry is related to the destruction of carbonaceous grains and PAHs. We detect a weak and broad absorption in the velocity range corresponding to the ISM along the sightline toward G10.62-0.4 as well as additional absorption features toward G5.89-0.4 and in the SgrB2 envelope near 60 km s^{-1} (Fig. 1). The achieved S/N is not sufficient for the QSO sight-lines, and the spectra toward our two SgrB2 targets are too crowded with multiple emission lines and spectral confusion with CH₃NH₂ for a derivation of C₃H⁺ column densities in the velocity components outside the SgrB2 envelope. The derived column densities reported in Table 3 are at the level of a few times 10^{11} cm^{-2} , very similar to the values found at the edge of the Horsehead nebula. C₃H⁺ is then about two times more abundant than HOC⁺, with a mean abundance ratio relative to HCO⁺ of $\sim 2.5\%$.

4. Molecular ion abundances

We report in Table 3 the column densities of the detected species in selected velocity intervals. We have also included column densities for the detected neutral species. The H₂O abundance refers to both ortho and para symmetry states. We first discuss the HCO⁺ abundance relative to H₂, using the *Herschel* CH absorption measurements (Gerin et al. 2010) to derive the H₂ column densities, and the well determined CH abundance relative to H₂, [CH] = 3.6×10^{-8} (Sheffer et al. 2008). Figure 4 presents the relative abundances of HCO⁺, HF, p-H₂O, and CCH as a function of the H₂ column density. For the QSO sight-lines, without CH data, the H₂ column density has been derived using the mean reddening E(B-V) from Schlegel et al. (1998) and with a correction for the atomic gas using H I absorption (Lucas & Liszt 1996). The *Herschel* and ALMA data are complemented by absorption data of HCO⁺ and CCH using the IRAM-30 m telescope (Godard et al. 2010; Gerin et al. 2011). Including the sight-lines towards W49N and W51 increases the sample size for a more robust statistics. These sight-lines have been shown to probe similar environments as those towards G10.62-0.4 and G5.89-0.4 (Gerin et al. 2015). In addition to the species discussed in this paper (HCO⁺, HF, and H₂O), we have included the CCH radical because it is closely chemically related to CH and as such is a potential tracer of molecular hydrogen in diffuse gas. Over a range of column densities spanning more than one order of magnitude, and for all sight-lines probing different environments, we confirm that the HCO⁺ abundance relative to H₂ remains fairly constant with a mean value of [HCO⁺] = 3.1×10^{-9} and a moderate scatter of 0.21 dex. HF and CCH also present nearly constant abundances relative to H₂ with moderate dispersions of about 0.15 dex.

Using the HCO⁺ abundance as reference, with [HCO⁺] = 3×10^{-9} , we list in Table 4 the abundances relative to H₂ of the HOC⁺, CF⁺, and C₃H⁺ molecular ions. We also recall the mean HF, CCH, H₂O, and OH abundances for the same sight-lines. The abundance of HF relative to H₂ has been directly

Table 4. Abundances relative to H₂.

Molecule	Abundance	Uncertainty dex	Comment	$N(\text{H}_2)/\int \tau dv$ $\text{cm}^{-2}/\text{km s}^{-1}$
HCO ⁺	3.1×10^{-9}	0.21	Using [CH] = 3.6×10^{-8} and E(B-V) ^e	4.0×10^{20}
HOC ⁺	4.6×10^{-11}	0.21	From [HOC ⁺]/[HCO ⁺]	5.2×10^{22}
CF ⁺	1.7×10^{-10}	0.30	From [CF ⁺]/[HCO ⁺]	9.0×10^{22}
C ₃ H ⁺	7.5×10^{-11}	0.30	From [C ₃ H ⁺]/[HCO ⁺]	2.0×10^{23}
HF	1.2×10^{-8}	0.14	Using [CH] = 3.6×10^{-8e}	2.0×10^{20}
H ₂ O ^a	2.7×10^{-8}	0.20	Using [CH] = 3.6×10^{-8e}	3.4×10^{20}
CCH	4.4×10^{-8}	0.15	Using [CH] = 3.6×10^{-8e}	1.5×10^{21}
CH ^b	3.6×10^{-8}	0.21	Sheffer et al. (2008)	1.0×10^{21}
CH ^c	3.6×10^{-8}	0.21	Sheffer et al. (2008)	9.7×10^{20}
OH ^d	1.0×10^{-7}	0.1	Weselak et al. (2010)	2.5×10^{20}

Notes. ^(a)The entry in the last column refers to the ground-state p-H₂O line at 1.13 THz and assume an ortho-to-para ratio of three. ^(b)The entry in the last column refers to the 532 or the 536 GHz transitions of CH. ^(c)The entry in the last column refers to the 2 THz transitions of CH. ^(d)The entry in the last column refers to the 2.5 THz transitions of OH. Weselak et al. (2010) present data for five objects only. ^(e)Sheffer et al. (2008).

determined toward the background star HD 154368 by Indriolo et al. (2013) to be $(1.15 \pm 0.4) \times 10^{-8}$ in agreement with the mean value listed in Table 4. This sight-line has $N(\text{HF})/N(\text{CH}) = 0.26 \pm 0.06$, close to the mean value determined in the far infrared with *Herschel*, 0.4 (Godard et al. 2012; Wiesemeyer et al. 2016).

The new ALMA data confirm previous measurements and expand the range of probed physical conditions. It is remarkable that the diffuse molecular gas, detected locally toward background QSOs, or in the Galactic Plane along sight-lines toward distant H II regions, presents rather uniform properties. The rare molecular ions CF⁺, HOC⁺, and C₃H⁺ reach abundances relative to H₂ of a few times 10⁻¹¹. The derived value for C₃H⁺ of $\sim 7 \times 10^{-11}$ is in good agreement with the abundance measured at the edge of the Horsehead nebula or the Orion Bar from C₃H⁺ emission lines (Pety et al. 2012; Cuadrado et al. 2015; Guzmán et al. 2015).

The homogeneity of the relative molecular abundances can be used to select the best diagnostics for detecting diffuse molecular gas in absorption. The last column of Table 4 lists the detectable H₂ column for an integrated opacity of the ground-state transition of 1 km s⁻¹ using the mean H₂ abundances listed in column 2 of the same Table. For comparison, the sensitivity of the CH ground-state transitions is $N(\text{H}_2)/\int \tau dv = 10^{21} \text{ cm}^{-2}/\text{km s}^{-1}$ for the 532 and 536 GHz lines and $9.7 \times 10^{20} \text{ cm}^{-2}/\text{km s}^{-1}$ for the stronger transitions near 2.0 THz now accessible with SOFIA (Wiesemeyer et al. 2018). We see that HF is the most sensitive tracer of diffuse molecular hydrogen, and that OH, p-H₂O, and HCO⁺ have comparable sensitivities of $N(\text{H}_2) \sim 3 - 4 \times 10^{20} \text{ cm}^{-2}$ for an integrated absorption of 1 km s⁻¹. For larger gas columns, when the ground-state transitions from this first set of species become saturated, CCH and CH, and then HOC⁺ can be used as probes of diffuse molecular gas. The millimeter lines from CF⁺ and C₃H⁺ appear too weak to be used as diagnostics of diffuse molecular gas.

5. Chemistry

The revised determinations of the molecular ion abundances, and the tight relationships between species provide new constraints on the formation and destruction pathways of the studied molecular ions. As discussed by Liszt et al. (2004), HOC⁺ in diffuse

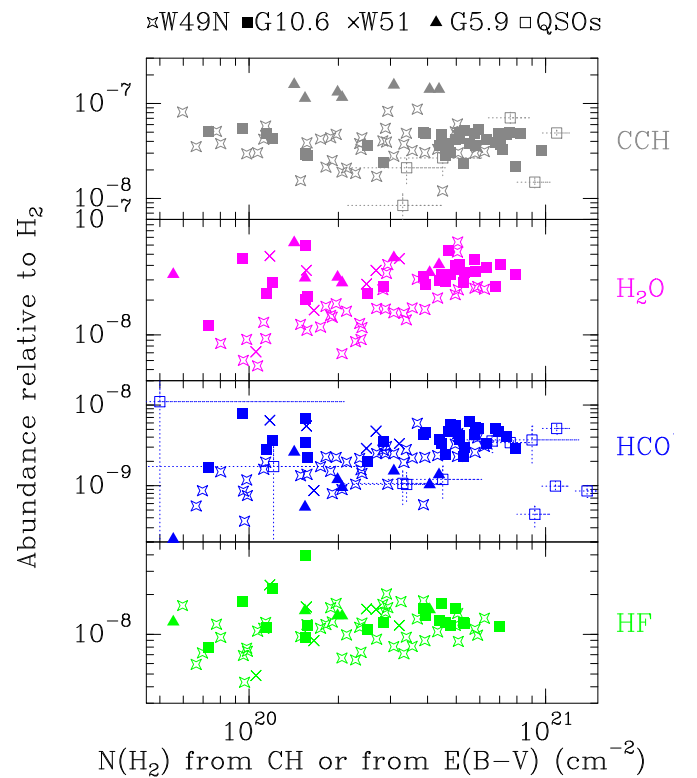


Fig. 4. Abundance relative to H₂ as a function of the H₂ column density derived from the submillimeter CH observations at 532 or 536 GHz or from the reddening. The different symbols refer to different sight-lines as noted at top. HCO⁺ is shown in blue, HF in green, H₂O in purple, and CCH in gray. The CCH data were taken with the IRAM-30 m telescope (Gerin et al. 2011) as well as the HCO⁺ data for W49N and W51 (Godard et al. 2010).

gas is mainly produced by the exothermic reaction between C⁺ and H₂O. This reaction also produces HCO⁺ but is thought to always be a minor formation pathway for this ion. A second production route for both HOC⁺ and HCO⁺ is the reaction between CO⁺ and H₂, CO⁺ itself being mostly formed in the reaction between C⁺ and OH. In diffuse cloud conditions, HCO⁺ and HOC⁺ are both destroyed by dissociative recombination with electrons, HOC⁺ is also destroyed in the isomerization reaction

with H_2 which produces HCO^+ , the two processes having similar rates. Following [Liszt et al. \(2004\)](#), and using the chemical scheme described in Appendix C, the ratios of the HOC^+ and H_2O abundances at steady state can be written:

$$\frac{[\text{HOC}^+]}{[\text{H}_2\text{O}]} = x_{\text{C}} \frac{2k_1(k'_e x_{\text{C}} + k_3 f(\text{H}_2)) + k_3 k_2 f(\text{H}_2)[\text{OH}]/[\text{H}_2\text{O}]}{(k'_e x_{\text{C}} + k_3 f(\text{H}_2))(2k_e x_{\text{C}} + k_4 f(\text{H}_2))}. \quad (11)$$

The behavior of this ratio with temperature and H_2 fraction is illustrated in Figs. C.1–C.3 in which we used the observed $[\text{OH}]/[\text{H}_2\text{O}]$ ratio (~ 4) quoted above, and two hypotheses for the rate coefficients, the Langevin rate or an enhanced capture rate at low temperature for ion–molecule reactions ([Woon & Herbst 2009](#)). The tight relationship between HOC^+ , OH and H_2O and the observed abundance ratio are qualitatively consistent with this simple chemical scheme. We note that the observed value of $N(\text{HOC}^+)/N(\text{H}_2\text{O}) \sim 2 \times 10^{-3}$ is in better agreement with the lower values of the rate coefficients, which do not include the enhancement of the capture rate in ion–polar molecule reactions. Because of the important role reactions (R1) between C^+ and H_2O , and (R2) between C^+ and OH play in initiating the diffuse gas chemistry, a better knowledge of their rate coefficients, their temperature dependence and branching ratios would be very beneficial.

It is not possible to understand the observed relationship between HCO^+ and H_2O with this simple chemical scheme because it predicts a significantly lower $[\text{HCO}^+]/[\text{H}_2\text{O}]$ abundance ratio than observed, in agreement with the existence of other, more dominant, chemical pathways for HCO^+ that are initiated by CH^+ and do not lead to HOC^+ ([Godard et al. 2009, 2014](#)). Whatever the chemical pathways that are involved, they must predict the tight relationship between HCO^+ and OH or H_2O . For instance, [Godard et al. \(2009\)](#) have shown that predicted HCO^+ and OH abundances by the turbulent dissipation regions (TDR) models satisfactorily reproduce the observed trend.

The last panel of Figs. C.2 and C.3 presents the expected abundance ratio $[\text{CF}^+]/[\text{HF}]$. The presence of detectable quantities of CF^+ was predicted by [Neufeld et al. \(2005\)](#), before its actual detection in the Orion Bar ([Neufeld et al. 2006](#)). As discussed previously ([Neufeld & Wolfire 2009; Guzmán et al. 2012; Liszt et al. 2014](#)), the CF^+ chemistry is very simple and, in diffuse gas where the electrons are produced by the ionization of carbon, the abundance ratio $[\text{CF}^+]/[\text{HF}]$ can be simply written as

$$[\text{CF}^+]/[\text{HF}] = k_5/kr_e = 0.053(T/70 \text{ K})^{0.65} \quad (12)$$

using the reaction rates from [Neufeld & Wolfire \(2009\)](#) as listed in Table C.1. Using instead the Langevin rate for the reaction R5 ($\text{C}^+ + \text{HF}$) leads to a very low value for $[\text{CF}^+]/[\text{HF}]$ of 0.5% at 70 K (see Fig. C.2). Using the enhanced capture rate for ion–molecule reactions leads to a rate coefficient of $\sim 5 \times 10^{-9} \text{ cm}^3 \text{ s}^{-1}$ at 100 K increasing with decreasing temperatures, and a predicted value of $[\text{CF}^+]/[\text{HF}]$ of 3.4% at 70 K (see Fig. C.1), in better agreement with the observations but still somewhat too high. A recent theoretical study has been presented by [Denis-Alpizar et al. \(2018\)](#) for the temperature range 50–2000 K. They predict a rate coefficient only moderately larger than the Langevin rate, which reaches $1.35 \times 10^{-9} \text{ cm}^3 \text{ s}^{-1}$ at 70 K and $1.22 \times 10^{-9} \text{ cm}^3 \text{ s}^{-1}$ at 100 K (see Table C.1). The corresponding $[\text{CF}^+]/[\text{HF}]$ ratio is 0.8%, a factor of two lower than the mean observed value, but still marginally consistent given the large uncertainties. Therefore, the data and the recent

Table 5. Summary of abundance ratios.

Ratio	Galactic Disk	SgrB2
		$V_{\text{LSR}} < -20 \text{ km s}^{-1}$
HF/p- H_2O	1.9 ± 0.4	0.43 ± 0.1
HCO^+ /p- H_2O	0.47 ± 0.03	0.37 ± 0.03
HCO^+ /HF	0.25 ± 0.02	0.88 ± 0.1
HOC^+ / HCO^+	$(1.5 \pm 0.2) \times 10^{-2}$	$(0.8 \pm 0.1) \times 10^{-2}$
CF^+ /HF	$(1.7 \pm 0.3) \times 10^{-2}$	$(3.0 \pm 0.3) \times 10^{-2}$

theoretical calculations agree that the rate coefficient of reaction R5 used by [Neufeld & Wolfire \(2009\)](#) is too high and should be revised downward by a factor of about $\sim 5.3/1.7\text{--}3$. A further test of the chemistry would be to search for variations of the abundance ratio with the temperature, but the current data quality are too marginal at this stage. The W49N sight-line is a promising target because of the relative spread in kinetic temperatures along the line of sight, with a cold and narrow velocity component near 40 km s^{-1} , prominent in CF^+ ([Gerin et al. 2015; Liszt et al. 2015](#)).

6. Material observed toward SgrA and SgrB2

Although sight-lines toward SgrA (G0.02-0.07) and SgrB2 were included in the observing program (Table 1), abundances in the material sampled along these directions were not included when deriving the relationships and abundances discussed in Sect. 3 and shown in Table 4. Gas seen in absorption at negative velocities toward SgrA and SgrB2 arises in the central molecular zone within about 200 pc of the Galactic center and exists under conditions of different (mostly higher) density, pressure, temperature, metallicity, and cosmic-ray ionization rate ([Morris & Serabyn 1996; Goto et al. 2014](#)). It is unclear whether any of the material observed along these lines of sight can be considered as diffuse molecular gas in the usual sense that is applicable to Galactic disk gas, that is being optically transparent and having moderate density and pressure ([Thiel et al. 2017; Liszt et al. 2018](#)).

Absolute abundances cannot be accurately determined because the abundances of the usual H_2 -tracers (CH , HF , HCO^+) with respect to H_2 have not been accurately established in the Galactic Center region. [Sonnentrucker et al. \(2013\)](#) have shown that H_2O and CH are enhanced relative to HF along sight-lines close to SgrA*, but not by the same factor (~ 5 for H_2O and ~ 2 for CH). It is therefore expected that the various molecular abundance ratios displayed in Table 5 reflect the differences in the physical conditions between the Galactic disk and the central molecular zone. The $N(\text{HOC}^+)/N(\text{HCO}^+)$ and $N(\text{HOC}^+)/N(\text{p-H}_2\text{O})$ ratios near the Galactic nucleus are 55% of what is seen in the disk, while the $N(\text{HCO}^+)/N(\text{p-H}_2\text{O})$ ratio also declines, but only by 30%. More extreme, [Sonnentrucker et al. \(2015\)](#) found that $N(\text{HF})/N(\text{H}_2\text{O})$ is a factor 4.4 smaller in the Galactic center and our data show a comparable decline by a factor 3.5 in the ratio $N(\text{HF})/N(\text{HCO}^+)$. By contrast, CF^+ seems to vary somewhat less between the disk and center: $N(\text{CF}^+)/N(\text{HOC}^+)$ is larger in the Galactic center by about the same factor by which $N(\text{HOC}^+)/N(\text{HCO}^+)$ declines, and $N(\text{CF}^+)/N(\text{HF})$ increases by 75%, consistent with the decline in $N(\text{HF})/N(\text{H}_2\text{O})$.

All things considered, the biggest surprise here may be the relative insensitivity of the chemistry to the strong differences in conditions that are supposed to occur near the Galactic

center. According to the discussion in Sect. 5 (see Fig. C.1), a lower $N(\text{HOC}^+)/N(\text{p-H}_2\text{O})$ ratio can be explained with a higher molecular fraction in the gas but the higher kinetic temperatures expected in the central molecular zone would have an opposite effect.

7. Summary and conclusions

Using ALMA Cycle 2 data we discussed observations of the molecular ions CF^+ , HCO^+ , HOC^+ , and C_3H^+ in absorption along inner-galaxy sight-lines toward a variety of background sources listed in Table 1: the distant quasar B1730-130 aka J1733-1304, two compact H II regions G5.89-0.4 and G10.62-0.38 in the galactic disk, and the H II regions SgrA G0.02-0.07, SgrB2-M, and SgrB2-S in the central molecular zone. Neutral species HCN, HNC, $\text{c-C}_3\text{H}$, NH_2CHO and ^{13}CS were also observed in the same program (Table 2, Fig. B.1) but were not discussed in any detail. Observations of absorption toward another quasar in the same observing program, B1741-312, were presented in a previous paper that discussed the molecular contribution from gas in the Galactic bulge, outside the central molecular zone (Gerin & Liszt 2017).

Spectra of the species we observed are shown in Fig. 1 and Fig. B.1. Figure 2 compares spectra of the ions HCO^+ and HOC^+ with those of HF and H_2O toward W31 G10.6-0.38, highlighting the strong similarity that was observed among the oxygen-bearing species in this work. Figure 3 shows spectral channel-by-channel graphs of the interrelationships among these species and with CF^+ whose abundance is proportional to that of HF. For future reference, Table 3 gives column densities for all observed species over selected velocity ranges toward all sources but the abundances of the neutral species observed here were not discussed in this paper.

Absorption originating in the central molecular zone and seen at negative velocities toward SgrA and SgrB2 has abundance patterns that differ from those of the Galactic disk gas, and was not included in the average molecular abundances and abundance ratios discussed in Sect. 3 and shown in Table 4. The Galactic disk and Galactic center abundances are summarized separately.

7.1. Gas in the Galactic disk

Using the known abundance of $N(\text{CH})/N(\text{H}_2) = 3.6 \times 10^{-8}$ and *Herschel* HiFi measurements of ground-state transitions of CH at 532 and 536 GHz, we compared HCO^+ and CH absorption profiles to derive the relative abundance $N(\text{HCO}^+)/N(\text{H}_2) = (3.1 \pm 1.9) \times 10^{-9}$, confirming the previously determined ratio 3×10^{-9} . We used this to determine the abundances of the other ions CF^+ , HOC^+ , and C_3H^+ relative to H_2 as shown in Table 4. Table 4 also gives the relative abundances of HF, H_2O , CCH, CH, and OH that were used as comparisons in discussion of the molecular chemistry.

C_3H^+ was found to be common in our sight-line sample in diffuse molecular gas in the Galactic disk, the first time this species has been seen outside the Orion A and Orion B photo-dissociation regions and the central molecular zone. The relative abundance $N(\text{C}_3\text{H}^+)/N(\text{H}_2) = 7.5 \times 10^{-11}$ is similar to that seen in Orion. Absorption by C_3H^+ is weak in the transition observed here and is contaminated by the spectra of other species especially toward SgrB2. This limits the usefulness of C_3H^+ as a general tracer but the constancy of its observed abundance should be further checked, and could provide a useful constraint on chemical modeling.

We also confirmed a lower CF^+ abundance $N(\text{CF}^+)/N(\text{H}_2) = 1.5 \times 10^{-10}$ than was originally predicted, and we ascribed it to a slow formation rate of the reaction $\text{C}^+ + \text{HF} \rightarrow \text{CF}^+ + \text{H}$ (Sect. 5) as recently calculated by Denis-Alpizar et al. (2018). Although CF^+ has a near-constant abundance with respect to the H_2 -tracer HF, absorption in the transition that we observed (Table 2) is weak and contaminated by an overlapping hydrogen recombination line toward H II regions, compromising its usefulness to trace H_2 .

The abundances and profiles of HOC^+ , HCO^+ and H_2O are tightly correlated in the Galactic disk gas (see Fig. 2), with $N(\text{HOC}^+)/N(\text{HCO}^+) = (1.5 \pm 0.3) \times 10^{-2}$ and $N(\text{HCO}^+)/N(\text{p-H}_2\text{O}) = 0.47 \pm 0.03$. The tight association of HCO^+ with the other two species is puzzling in that the abundance of HCO^+ in the diffuse gas requires a turbulent-dissipative formation chemistry (Godard et al. 2014) and the channel that forms HCO^+ in the reaction of C^+ and H_2O is not an important source of HCO^+ , while the $\text{HOC}^+/\text{H}_2\text{O}$ ratio is best explained by the reaction of C^+ and H_2O at Langevin rates (Sect. 5 and Fig. C.1) and the column densities of water are also explained by the quiescent chemistry. The rate coefficients of the reactions between C^+ and OH and H_2O have an important effect on the predicted chemical abundances and their absolute value and temperature dependence should be more accurately known.

7.2. Gas observed toward SgrB2

Gas seen in absorption at negative velocities toward SgrA and SgrB2 arises in the central molecular zone within 200 pc of the Galactic center and exists under conditions of different (mostly higher) density, pressure, temperature, metallicity and cosmic-ray ionization rate as discussed in Sect. 6. This is presumably reflected in the molecular abundance ratios that differ from those in the galactic disk by as much as a factor two for the $N(\text{HOC}^+)/N(\text{HCO}^+)$ ratio or 4 for $N(\text{HF})/N(\text{H}_2\text{O})$ and $N(\text{HF})/N(\text{HCO}^+)$. Absolute abundances cannot be determined in the central molecular zone because the relative abundances of the usual H_2 -tracers (CH, HF, etc.) have not been established in this region, and it is unclear whether any of the gas in the central molecular zone is diffuse in the sense that is usually understood in the Galactic disk, being optically transparent and having moderate density and pressure. The spectra of CF^+ and C_3H^+ are contaminated along the galactic center sight-lines where the optical depths of abundant species like HF and HCO^+ are high, complicating the derivation of accurate molecular abundances.

Acknowledgements. This paper makes use of the following ALMA data: ADS/JAO.ALMA#2013.1.01194.S. ALMA is a partnership of ESO (representing its member states), NSF (USA), and NINS (Japan), together with NRC (Canada), NSC, and ASIAA (Taiwan), and KASI (Republic of Korea), in cooperation with the Republic of Chile. The Joint ALMA Observatory is operated by ESO, AUI/NRAO and NAOJ. The National Radio Astronomy Observatory is a facility of the National Science Foundation operated under cooperative agreement by Associated Universities, Inc. We acknowledge funding support from PCMI-CNRS/INSU and AS ALMA from Observatoire de Paris. We thank E. Bergin and E. Falgarone for illuminating discussions, and the referee for a careful reading of the manuscript.

References

- Cuadrado, S., Goicoechea, J. R., Pilleri, P., et al. 2015, *A&A*, 575, A82
 Denis-Alpizar, O., Guzmán, V. V., & Inostroza, N. 2018, *MNRAS*, 479, 753
 Flagey, N., Goldsmith, P. F., Lis, D. C., et al. 2013, *ApJ*, 762, 11
 Gerin, M., & Liszt, H. 2017, *A&A*, 600, A48
 Gerin, M., de Luca, M., Goicoechea, J. R., et al. 2010, *A&A*, 521, L16
 Gerin, M., Kaźmierczak, M., Jastrzebska, M., et al. 2011, *A&A*, 525, A116

- Gerin, M., Ruaud, M., Goicoechea, J. R., et al. 2015, *A&A*, 573, A30
- Gerin, M., Neufeld, D. A., & Goicoechea, J. R. 2016, *ARA&A*, 54, 181
- Godard, B., Falgarone, E., & Pineau Des Forêts, G. 2009, *A&A*, 495, 847
- Godard, B., Falgarone, E., Gerin, M., Hily-Blant, P., & de Luca, M. 2010, *A&A*, 520, A20
- Godard, B., Falgarone, E., Gerin, M., et al. 2012, *A&A*, 540, A87
- Godard, B., Falgarone, E., & Pineau des Forêts, G. 2014, *A&A*, 570, A27
- Goss, W. M. 1968, *ApJS*, 15, 131
- Goto, M., Geballe, T. R., Indriolo, N., et al. 2014, *ApJ*, 786, 96
- Green, G. M., Schlafly, E. F., Finkbeiner, D. P., et al. 2015, *ApJ*, 810, 25
- Guzmán, V., Pety, J., Gratier, P., et al. 2012, *A&A*, 543, L1
- Guzmán, V. V., Pety, J., Goicoechea, J. R., et al. 2015, *ApJ*, 800, L33
- Hamberg, M., Kashperkat, I., Thomas, R. D., et al. 2014, *J. Phys. Chem. A.*, 118, 6034
- Indriolo, N., Neufeld, D. A., Seifahrt, A., & Richter, M. J. 2013, *ApJ*, 764, 188
- Jenkins, E. B., & Tripp, T. M. 2011, *ApJ*, 734, 65
- Lallement, R., Vergely, J.-L., Valette, B., et al. 2014, *A&A*, 561, A91
- Liszt, H. S., & Gerin, M. 2016, *A&A*, 585, A80
- Liszt, H., Lucas, R., & Black, J. H. 2004, *A&A*, 428, 117
- Liszt, H. S., Pety, J., Gerin, M., & Lucas, R. 2014, *A&A*, 564, A64
- Liszt, H. S., Guzmán, V. V., Pety, J., et al. 2015, *A&A*, 579, A12
- Liszt, H., Gerin, M., Beasley, A., & Pety, J. 2018, *ApJ*, 856, 151
- Lucas, R., & Liszt, H. 1996, *A&A*, 307, 237
- Martinez, Jr., O., Betts, N. B., Villano, S. M., et al. 2008, *ApJ*, 686, 1486
- McGuire, B. A., Carroll, P. B., Loomis, R. A., et al. 2013, *ApJ*, 774, 56
- Morris, M., & Serabyn, E. 1996, *ARA&A*, 34, 645
- Müller, H. S. P., Belloche, A., Xu, L.-H., et al. 2016, *A&A*, 587, A92
- Neufeld, D. A., & Wolfire, M. G. 2009, *ApJ*, 706, 1594
- Neufeld, D. A., Kaufman, M. J., Goldsmith, P. F., Hollenbach, D. J., & Plume, R. 2002, *ApJ*, 580, 278
- Neufeld, D. A., Wolfire, M. G., & Schilke, P. 2005, *ApJ*, 628, 260
- Neufeld, D. A., Schilke, P., Menten, K. M., et al. 2006, *A&A*, 454, L37
- Neufeld, D. A., Godard, B., Gerin, M., et al. 2015, *A&A*, 577, A49
- Novotny, O., Mitchell, J. B. A., LeGarrec, J. L., et al. 2005, *J. Phys. B At. Mol. Phys.*, 38, 1471
- Pearson, J. C., Brauer, C. S., & Drouin, B. J. 2008, *J. Mol. Spectr.*, 251, 394
- Pety, J., Gratier, P., Guzmán, V., et al. 2012, *A&A*, 548, A68
- Pineda, J. L., Langer, W. D., Velusamy, T., & Goldsmith, P. F. 2013, *A&A*, 554, A103
- Planck Collaboration XXIV. 2011, *A&A*, 536, A24
- Plume, R., Kaufman, M. J., Neufeld, D. A., et al. 2004, *ApJ*, 605, 247
- Rachford, B. L., Snow, T. P., Destree, J. D., et al. 2009, *ApJS*, 180, 125
- Remy, Q., Grenier, I. A., Marshall, D. J., & Casandjian, J. M. 2017, *A&A*, 601, A78
- Schlegel, D. J., Finkbeiner, D. P., & Davis, M. 1998, *ApJ*, 500, 525
- Sheffer, Y., Rogers, M., Federman, S. R., et al. 2008, *ApJ*, 687, 1075
- Smith, M. A., Schlemmer, S., von Richthofen, J., & Gerlich, D. 2002, *ApJ*, 578, L87
- Snow, T. P., & McCall, B. J. 2006, *ARA&A*, 44, 367
- Sonnentrucker, P., Neufeld, D. A., Gerin, M., et al. 2013, *ApJ*, 763, L19
- Sonnentrucker, P., Wolfire, M., Neufeld, D. A., et al. 2015, *ApJ*, 806, 49
- Spitzer, Jr., L., & Jenkins, E. B. 1975, *ARA&A*, 13, 133
- Stoffels, A., Kluge, L., Schlemmer, S., & Brünken, S. 2016, *A&A*, 593, A56
- Thiel, V., Belloche, A., Menten, K. M., Garrod, R. T., & Müller, H. S. P. 2017, *A&A*, 605, L6
- Wakelam, V., Herbst, E., Loison, J.-C., et al. 2012, *ApJS*, 199, 21
- Weselak, T., Galazutdinov, G. A., Beletsky, Y., & Krelowski, J. 2010, *MNRAS*, 402, 1991
- Whiteoak, J. B., & Gardner, F. F. 1970, *Astrophys. Lett.*, 5, 5
- Wiesemeyer, H., Güsten, R., Heyminck, S., et al. 2016, *A&A*, 585, A76
- Wiesemeyer, H., Güsten, R., Menten, K. M., et al. 2018, *A&A*, 612, A37
- Wolfire, M. G., Hollenbach, D., & McKee, C. F. 2010, *ApJ*, 716, 1191
- Woon, D. E., & Herbst, E. 2009, *ApJS*, 185, 273

Appendix A: Continuum images

Figure A.1 presents the continuum images at 102 GHz obtained with ALMA.

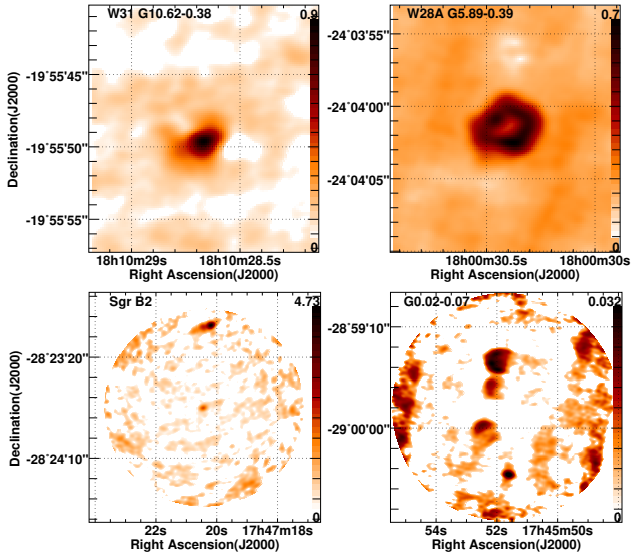


Fig. A.1. Continuum images at 102 GHz obtained with ALMA. The color bar shows the intensity scale in Jy beam^{-1} for W31C(G10.6-0.4), W28A2 (G5.89-0.4), SgrB2 and G0.02-0.07 with the peak value given at the top of the color bar. In the SgrB2 image, the source in the middle is the SgrB2-S H II region and the strong source at the top is SgrB2-M.

Appendix B: Spectra

Figure B.1 presents the whole set of absorption spectra.

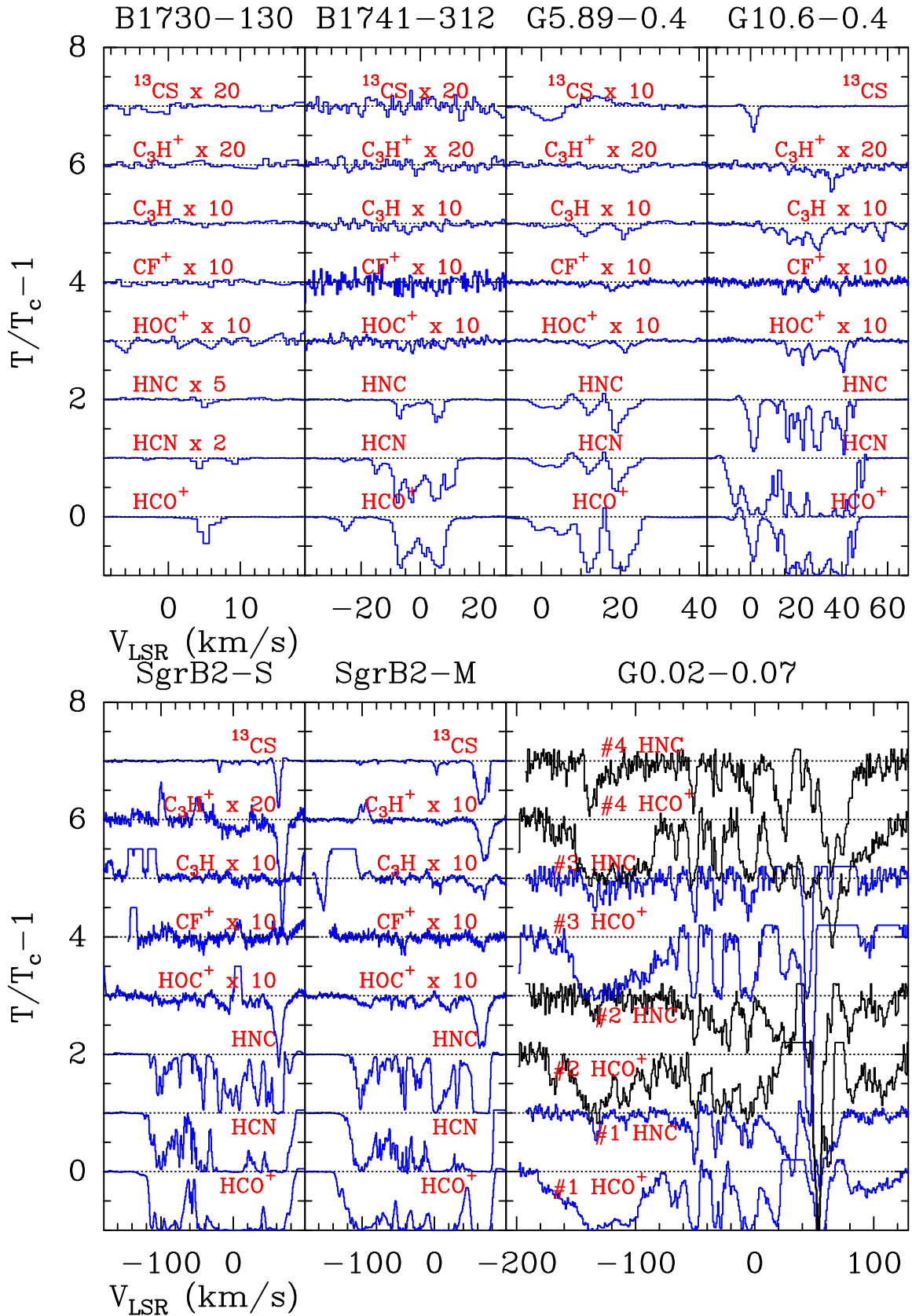


Fig. B.1. Absorption spectra obtained with ALMA. The spectra are plotted as baseline subtracted line/continuum data. They have been vertically shifted and clipped for clarity. Toward G0.02-0.07 data are displayed toward four positions that correspond to the brightest continuum peaks: #1 at 17:45:51.9, -28:59:27.3; #2 at 17:45:52.1, -28:59:40.8; #3 at 17:45:52.4, -29:00:03.5; #4 at 17:45:51.6, -29:00:22.8.

Appendix C: Chemistry

Table C.1. Main reactions considered.

Reaction	Rate coefficient (cm ³ s ⁻¹)	Reference and Comment
R1 : C ⁺ + H ₂ O → HCO ⁺ + H ; HOC ⁺ + H	$k_1 = k_L(0.4767 \frac{\mu_D}{\sqrt{2\alpha k_B T}} + 0.62)$	(1)(2) HOC ⁺ preferred, $k_L = 1.04 \times 10^{-9}$ cm ³ s ⁻¹
R2 : C ⁺ + OH → CO ⁺ + H	$k_2 = k_L(0.4767 \frac{\mu_D}{\sqrt{2\alpha k_B T}} + 0.62)$	(2)(3) $k_L = 9.1 \times 10^{-10}$ cm ³ s ⁻¹
R3 : CO ⁺ + H ₂ → HCO ⁺ + H; HOC ⁺ + H	$k_3 = 7.0 \times 10^{-10}$	(3) HOC ⁺ and HCO ⁺ produced equally
R4 : HOC ⁺ + H ₂ → HCO ⁺ + H ₂	$k_4 = 4.0 \times 10^{-10}$	(4)
R5 : C ⁺ + HF → CF ⁺ + H	$k_5 = 7.2 \times 10^{-9}(T/300)^{-0.15}$	(5) $k_L = 7.65 \times 10^{-10}$ cm ³ s ⁻¹
R5 : C ⁺ + HF → CF ⁺ + H	$k_5 = 8.64 \times 10^{-10}(T/300)^{-0.43}e^{-12.64/T}$	(6) $k_L = 7.65 \times 10^{-10}$ cm ³ s ⁻¹
R6 : HOC ⁺ + e ⁻ → CO + H	$k_e = 2.0 \times 10^{-7}(T/300)^{-0.75}$	(3)
R7 : HCO ⁺ + e ⁻ → CO + H	$k_e'' = 2.8 \times 10^{-7}(T/300)^{-0.69}$	(7)
R8 : CO ⁺ + e ⁻ → C + O	$k_e' = 2.75 \times 10^{-7}(T/300)^{-0.55}$	(3)
R9 : CF ⁺ + e ⁻ → C + F	$kr_e = 5.2 \times 10^{-8}(T/300)^{-0.8}$	(8)

Notes. (1) [Martinez et al. \(2008\)](#) measured $k_1 = 2.1 \times 10^{-9}$ cm³ s⁻¹ at 300 K, (2) [Woon & Herbst \(2009\)](#), (3) KIDA, (4) [Smith et al. \(2002\)](#), (5) [Neufeld & Wolfire \(2009\)](#), (6) [Denis-Alpizar et al. \(2018\)](#) the expression is valid for $50 \text{ K} \leq T \leq 2000 \text{ K}$, (7) [Hamberg et al. \(2014\)](#), (8) [Novotny et al. \(2005\)](#).

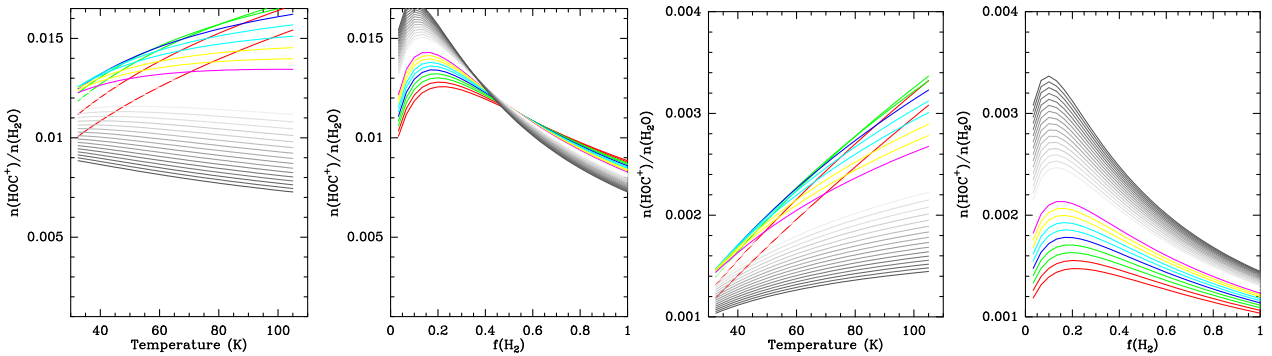


Fig. C.1. *Left panel:* variation of the ratio of the HOC⁺ and H₂O abundance with the kinetic temperature. Each curve represents a different fraction of hydrogen in molecular form $f(\text{H}_2)$ from 0.03 (red) up to 1 (black). *Right panel:* variation of the ratio of the HOC⁺ and H₂O abundance with $f(\text{H}_2)$. Each curve represents a different temperature from 32 K (red) up to 105 K (black). The two panels on the left use enhanced capture rates for reactions between ions and polar molecules using the formalism and the molecular data described by [Woon & Herbst \(2009\)](#). The *right panels* use the Langevin rates computed from the molecular data listed by [Woon & Herbst \(2009\)](#). The observed $N(\text{HOC}^+)/N(\text{H}_2\text{O})$ ratio is 1.8×10^{-3} , see [Table 5](#).

This section describes the analytical formulae used to compute steady state abundances for HOC⁺ and CF⁺. The main formation and destruction routes for HOC⁺ and CF⁺ are listed in [Table C.1](#) in which we quote the rates for HOC⁺ production, i.e. including the branching ratios. The reaction rate coefficients have been taken from the online database KIDA⁴ ([Wakelam et al. 2012](#)) and completed by additional references from the literature as indicated in [Table C.1](#).

As presented by [Liszt et al. \(2004\)](#), the main formation reactions for HOC⁺ is reaction R1, with a secondary contribution from reaction R3. For destruction, we only consider the dissociative recombination with electrons (Reaction R6) and the isomerization reaction with H₂ which transforms HOC⁺ in HCO⁺ (Reaction R4). We can therefore write the HOC⁺ formation rate as

$$\frac{dn(\text{HOC}^+)}{dt}_{\text{form}} = k_1 n(\text{C}^+) n(\text{H}_2\text{O}) + k_3 n(\text{CO}^+) n(\text{H}_2) \quad (\text{C.1})$$

and the destruction rate as

$$\frac{dn(\text{HOC}^+)}{dt}_{\text{dest}} = k_e n(\text{HOC}^+) n(\text{e}^-) + k_4 n(\text{HOC}^+) n(\text{H}_2). \quad (\text{C.2})$$

We further assume that C⁺ is the main carrier of carbon and all electrons are provided by C⁺, which leads to

$$n(\text{C}^+) = n(\text{e}^-) = x_C n_H = 2x_C n(\text{H}_2)/f(\text{H}_2), \quad (\text{C.3})$$

where we have introduced the fraction of hydrogen in molecular form, $f(\text{H}_2) = \frac{2n(\text{H}_2)}{n(\text{HI}) + 2n(\text{H}_2)}$, and $n_H = n(\text{HI}) + 2n(\text{H}_2)$, and the carbon abundance relative to H, x_C .

Equating the formation and destruction rates for HOC⁺, and writing $n(\text{H}_2\text{O}) = [\text{H}_2\text{O}]n(\text{H}_2)$, where $[\text{H}_2\text{O}]$ represents the abundance of water relative to H₂, we get

$$[\text{HOC}^+] = \frac{n(\text{HOC}^+)}{n(\text{H}_2)} = \frac{2k_1 x_C [\text{H}_2\text{O}] + k_3 [\text{CO}^+] f(\text{H}_2)}{2k_e x_C + k_4 f(\text{H}_2)}. \quad (\text{C.4})$$

CO⁺ is formed in reaction R2 and destroyed by reacting with electrons (R8) and with H₂ (R3). We therefore obtain the CO⁺

⁴ <http://kida.obs.u-bordeaux1.fr/>

abundance relative to H_2 , $[\text{CO}^+]$, in a similar way, where $[\text{OH}]$ represents the abundance of OH relative to H_2 :

$$[\text{CO}^+] = \frac{k_2 x_C [\text{OH}]}{k'_e x_C + k_3 f(\text{H}_2)}. \quad (\text{C.5})$$

By substituting $[\text{CO}^+]$, we obtain an equation for the ratio of the HOC^+ and H_2O abundances:

$$\frac{[\text{HOC}^+]}{[\text{H}_2\text{O}]} = x_C \frac{2k_1(k'_e x_C + k_3 f(\text{H}_2)) + k_3 k_2 f(\text{H}_2) \frac{[\text{OH}]}{[\text{H}_2\text{O}]}}{(k'_e x_C + k_3 f(\text{H}_2)) (2k_e x_C + k_4 f(\text{H}_2))}. \quad (\text{C.6})$$

We can also predict the ratio of HCO^+ and H_2O abundances using the same chemical network, noting α the small branching ratio toward HCO^+ in reaction R1:

$$\frac{[\text{HCO}^+]}{[\text{H}_2\text{O}]} = \frac{2k_1 \alpha (k'_e x_C + k_3 f(\text{H}_2)) + k_3 k_2 f(\text{H}_2) \frac{[\text{OH}]}{[\text{H}_2\text{O}]} + k_4 f(\text{H}_2) \frac{[\text{HOC}^+]}{[\text{H}_2\text{O}]}}{2k'_e x_C (k'_e x_C + k_3 f(\text{H}_2))}. \quad (\text{C.7})$$

Figures C.1 and C.2 illustrate the expected variation of the ratio of the HOC^+ and H_2O abundances with the kinetic temperature and with the fraction of hydrogen in molecular form $f(\text{H}_2)$. We used two assumptions for reactions R1, R2, and R5: the pure capture model (the Langevin rate), and the ion–molecule capture rate which leads to higher value and a strong temperature dependence (Woon & Herbst 2009). In this approach, the reaction rate can be written: $k = k_L(0.4767x + 0.62)$, where $x = \frac{\mu_D}{\sqrt{2\alpha k_B T}}$, μ_D is the dipole moment of the polar molecule, α is the polarizability, and T is the kinetic temperature. The formula is valid for $x \geq 2$, which is the case for the reactions considered in this work.

Martinez et al. (2008) have studied the $\text{C}^+ + \text{H}_2\text{O}$ reaction experimentally at 300 K using a flowing afterglow-selected ion flow tube (FASIFT). They determine a total rate of $2.1 \times 10^{-9} \text{ cm}^3 \text{ s}^{-1}$, a factor of 2 higher than the Langevin rate. The branching ratios between HCO^+ and HOC^+ are unknown.

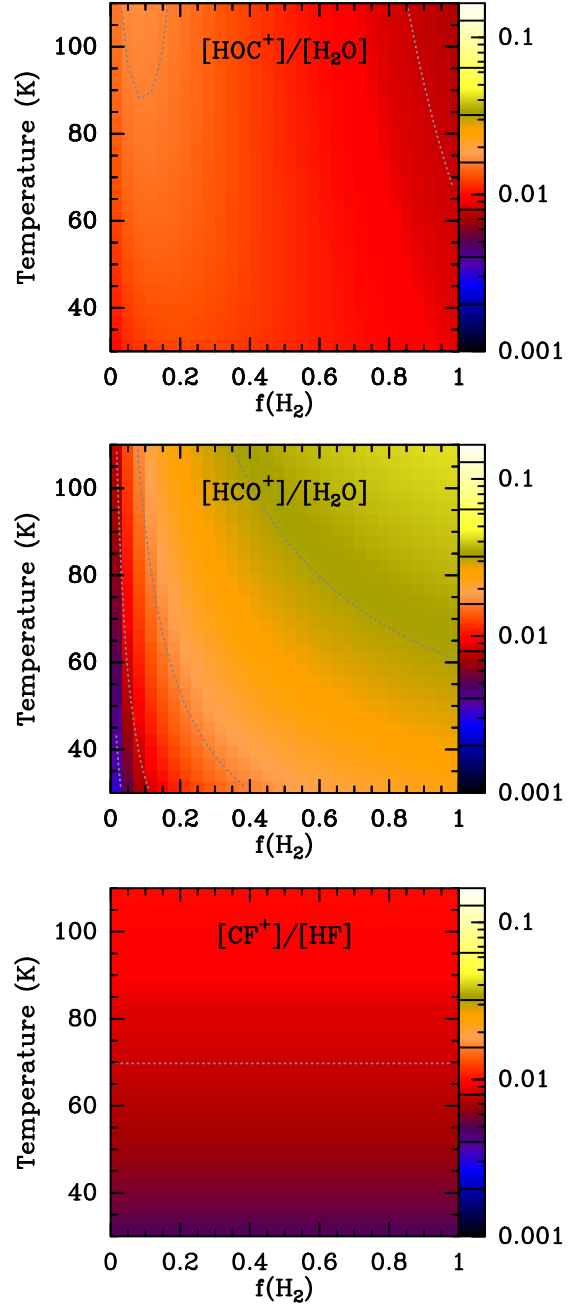


Fig. C.2. Variation of the predicted abundance ratios $[\text{HOC}^+]/[\text{H}_2\text{O}]$, $[\text{HCO}^+]/[\text{H}_2\text{O}]$, and $[\text{CF}^+]/[\text{HF}]$ as a function of the fraction of molecular gas $f(\text{H}_2)$ and the kinetic temperature. The plot is using enhanced capture rates for reactions between ions and polar molecules using the formalism and the molecular data described by Woon & Herbst (2009) and the new theoretical reaction rate for reaction R5 (Denis-Alpizar et al. 2018). Contour levels are set at 2×10^{-3} , 4×10^{-3} , 8×10^{-3} , ... up to 128×10^{-3} . The mean values of the abundance ratios are listed in Table 5.

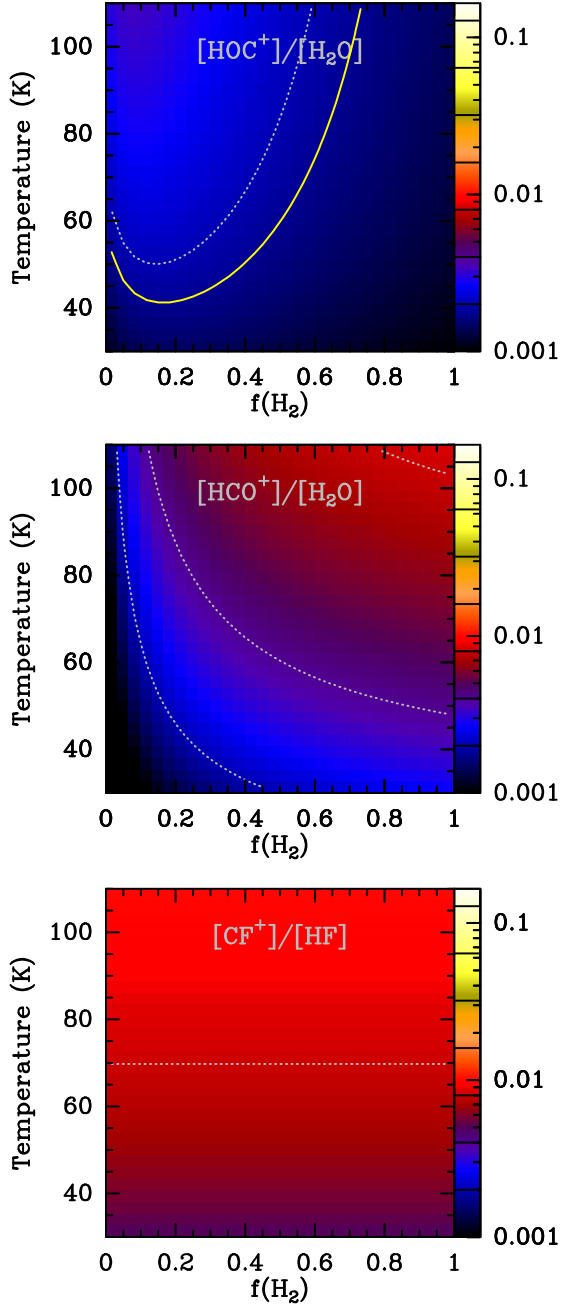


Fig. C.3. Variation of the predicted abundance ratios $[\text{HOC}^+]/[\text{H}_2\text{O}]$, $[\text{HCO}^+]/[\text{H}_2\text{O}]$, and $[\text{CF}^+]/[\text{HF}]$ as functions of the fraction of molecular gas $f(\text{H}_2)$ and the kinetic temperature. The plot uses Langevin rates for reactions between ions and polar molecules with the molecular data listed by [Woon & Herbst \(2009\)](#) and the new theoretical reaction rate for reaction R5 ([Denis-Alpizar et al. 2018](#)). Contour levels are set at 2×10^{-3} , 4×10^{-3} , 8×10^{-3} , ... up to 128×10^{-3} . The yellow contour in the top left box indicates the mean observed ratio $[\text{HOC}^+]/[\text{H}_2\text{O}] = 1.8 \times 10^{-3}$. The mean values of the abundance ratios are listed in [Table 5](#).